RAA 2017 Vol. **17** No. **8**, 80 (16pp) doi: 10.1088/1674–4527/17/8/80

http://www.raa-journal.org *http://iopscience.iop.org/raa*

***R**esearch in*
***A**stronomy and*
***A**strophysics*

p-capture reaction cycles in rotating massive stars and their impact on elemental abundances in globular cluster stars: A case study of O, Na and Al

Upakul Mahanta[1], Aruna Goswami[2], Hiralal Duorah[3] and Kalpana Duorah[4]

[1] Department of Physics, Bajali College, Pathsala, PIN 781325, India; *upakulmahanta@gmail.com*
[2] Indian Institute of Astrophysics, Bengaluru, PIN 560034, India; *aruna@iiap.res.in*
[3] Department of Physics, Gauhati University, Guwahati, PIN 781014, India; *hl_duorah@yahoo.com*
[4] Department of Physics, Gauhati University, Guwahati, PIN 781014, India; *khowang56@yahoo.co.in*

Received 2016 August 25; accepted 2017 April 21

Abstract Elemental abundance patterns of globular cluster stars can provide important clues for understanding cluster formation and early chemical evolution. The origin of the abundance patterns, however, still remains poorly understood. We have studied the impact of p-capture reaction cycles on the abundances of oxygen, sodium and aluminium considering nuclear reaction cycles of carbon-nitrogen-oxygen-fluorine, neon-sodium and magnesium-aluminium in massive stars in stellar conditions of temperature range 2×10^7 to 10×10^7 K and typical density of 10^2 gm cc^{-1}. We have estimated abundances of oxygen, sodium and aluminium with respect to Fe, which are then assumed to be ejected from those stars because of rotation reaching a critical limit. These ejected abundances of elements are then compared with their counterparts that have been observed in some metal-poor evolved stars, mainly giants and red giants, of globular clusters M3, M4, M13 and NGC 6752. We observe an excellent agreement with [O/Fe] between the estimated and observed abundance values for globular clusters M3 and M4 with a correlation coefficient above 0.9 and a strong linear correlation for the remaining two clusters with a correlation coefficient above 0.7. The estimated [Na/Fe] is found to have a correlation coefficient above 0.7, thus implying a strong correlation for all four globular clusters. As far as [Al/Fe] is concerned, it also shows a strong correlation between the estimated abundance and the observed abundance for globular clusters M13 and NGC 6752, since here also the correlation coefficient is above 0.7 whereas for globular cluster M4 there is a moderate correlation found with a correlation coefficient above 0.6. Possible sources of these discrepancies are discussed.

Key words: Galaxy: globular cluster: individual (M3, M4, M13, NGC 6752) — stars: abundances — stars: massive

1 INTRODUCTION

Globular cluster (GC) stars are known to display homogeneous abundance patterns for Fe-peak elements but significant abundance variations are seen among the light elements. Na-O and Mg-Al anticorrelations are also observed among the stars in GCs (Kraft et al. 1997; Gratton et al. 2004; Carretta et al. 2009; Smolinski et al. 2011 and references therein). Inhomogeneities and abundance variations observed in light-elements increase with decreasing metallicity. For instance, C, N, O and Na abundances in giants of M7 with an average metallicity ([Fe/H]) of ~ -0.7 show mild variations compared to their counterparts observed in giants of M5 with a metallicity of ~ -1.2. Several studies, both observational and theoretical, in literature are devoted to understanding the complex abundance patterns of GCs (Cordero et al. 2015; Roederer et al. 2016; Spite et al. 2016; Villanova et al. 2016). The origins of these observed abundance anomalies, however, still remain poorly understood. GCs span a wide range in metallicities with [Fe/H] as small as -2.38 up to as large as $+0.12$ (table 2 in Gratton et al. (2004) and references therein). Here among the chosen

GCs, GC M3 has an average metallicity of -1.39 and is more distant than M5. The scatter among light elements and the enhanced odd atomic numbered elements typically seen in metal-poor GCs are also noticed in M3, although at a lower level of star-to-star variation (Cohen & Meléndez 2005). GC M13 with an average metallicity of -1.50 is known to show large star-to-star differences in the abundance of Al, Mg, Na and O among its red giants (Cohen & Meléndez 2005 references therein). GC M4 is the closest to us (Dixon & Longmore 1993) and has an average cluster metallicity of -1.17 (Liu & Janes 1990; Drake et al. 1992, 1994). A characteristic feature observed in the color-magnitude diagrams of GC M4 stars is the presence of broadened red-giant branches (Marino et al. 2008). The two giant branches appear to correlate with typical GC variations in [O/Fe] and [Na/Fe] abundances rather than variations in total [C+N+O/Fe] abundance (Martell et al. 2011). Detailed elemental abundances are available for a large number of stars belonging to this cluster. The largest spread in light element abundances is known to be observed in GC NGC 6752. This GC has been studied by many groups including Yong et al. (2005), and the reported average cluster metallicity due to Yong et al. (2005) is ~ -1.61. But the common feature of these four GCs is the observed Na-O and Mg-Al anti-correlation. Proton-capture chains that convert C and O to N, Ne to Na and Mg into Al in the hydrogen-burning layers of evolved stars are believed to be responsible for these observed trends; however, the astrophysical site(s) for their occurrence is still under debate. Among the contested scenarios, one is *evolutionary* which considers deep mixing of the stellar envelope through the hydrogen burning shell that brings products of proton-capture chains to the surface. The other one is *primordial* where observed abundances originating from proton-capture synthesis that took place in some earlier generation of massive stars whose interior could easily attain a high temperature so that advanced H-burning could be sustained. However, recent spectroscopic studies have challenged the former one as it cannot possibly explain why a similar kind of abundance anomaly is present even in stars which are below and above the main sequence turn-off (Decressin et al. 2007b). Also, the evolutionary scenario cannot explain why stars in GC ω Cen, which is the most massive GC in the Milky Way, have been found with a large spread in metallicity, thereby discarding the earlier paradigm that the GCs are examples of "Simple Stellar Populations" (D'Ercole et al. 2008). Under the currently favored astrophysical sites where the processing of elements takes place, as well as the mechanism by which processed material is subsequently delivered into new generations of stars are (i) massive asymptotic giant branch (AGB) stars (D'Ercole et al. 2008), (ii) fast-rotating massive main sequence stars (Decressin et al. 2007b) and (iii) massive interacting binaries (de Mink et al. 2009). During Hot Bottom Burning (HBB) that occurs in AGB stars, the CNO elements undergo p-capture nucleosynthesis which is found to be sensitive to the metallicity of the star (Ventura et al. 2013). But this HBB, for any effective depletion of oxygen abundance due to p-capture reaction, requires a temperature as high as $T_9 > 0.1$ (Ventura et al. 2013). Again at high temperature the destruction channel for sodium is dominant compared to the production reaction by p-capture on ^{22}Ne nuclei, thus the sodium that previously accumulated at the surface is destroyed (Denissenkov & Herwig 2003; Ventura et al. 2013). This points towards correlation between Na and O abundance which in fact has been confirmed by a recent study performed by Ventura et al. (2013) at very low metallicity unless the polluted material that is lost from the surface of the stars via slow winds suffers a certain amount of dilution (Ventura et al. 2013). This leads to an Na-O anticorrelation and the materials then remain trapped within the gravitational potential of the cluster. As mentioned earlier, these four GCs have shown an Na-O anticorrelation, three of which have already been reported in a recent study performed by D'Antona & Ventura (2007) who considered some new stellar models. In the third scenario, interacting massive binary stars may provide an efficient way to lose large amounts of processed material that could be incorporated into an enriched population (de Mink et al. 2009). This scenario is attractive because a large fraction of massive stars are indeed observed to be members of binaries that will interact during their lifetime (Sana et al. 2013). de Mink et al. (2009) assumed a non-conservative evolution of massive close binaries which may not be correct because the mass that is lost by the loser (the primary one) leaves the binary as a slow wind driven by rotation of the gainer (the secondary one) and takes specific orbital angular momentum of the gainer. Thus this will lead to a merger of the binary and the evolution will be different as suggested by the same author (Vanbeveren et al. 2012). In the "winds from fast rotating massive stars" scenario (discussed in Section 2), it is assumed that massive stars within GCs rotate near break-up velocity. Processed material is brought to the surface by rotational mixing, lost via a mechanical wind, and then

accumulates in a disk around the star, where the second generation of (low-mass) stars is assumed to form (Decressin et al. 2010).

In this work we have considered the nuclear burning cycles carbon-nitrogen-oxygen-fluorine (CNOF), neon-sodium (NeNa) and magnesium-aluminium (MgAl) in a rotating massive star at high temperature and low density conditions and have estimated the abundances of the product elements O, Na and Al in a temperature range of 2×10^7 to 10×10^7 K since the CNO, NeNa and MgAl cycles are activated above temperatures 0.02×10^9 K, 0.035×10^9 K and 0.05×10^9 K respectively (Decressin et al. 2007b). Although nucleosynthesis during NeNa and MgAl cycles is discussed at length in Arnould et al. (1999) and José et al. (1999), the availability of new estimates of the cross-sections for many of the reactions involved in these cycles, from recent experimental determination (Iliadis et al. 2010), prompted us to reinvestigate the synthesis of elements due to these cycles. Our aim is to compute the abundances of key elements O, Na and Al, which are important diagnostics for understanding the associated chemical evolution, and thereby examine the impact of proton-capture reactions on the observed abundances of GC stars. A comparison between the computed and observed data suggests contributions coming from other sources, yet to be identified, that might have possibly influenced the observed abundances.

In Section 2 we present the physical conditions for the occurrence of nuclear burning cycles and lifetime measurements for proton-capture reactions. The evolution of stable elements in the cycles at equilibrium due to hydrogen burning is presented in Section 3. Section 4 deals with CNOF and other nuclear burning cycles and the abundance calculation of selected elements. Discussion and concluding remarks are presented in Section 5.

2 THE PHYSICAL SITUATION

Classical models of stellar evolution focus on the dominant role of various stages of nuclear burning in the stellar core. Not only is the temperature crucial in any stellar situation, but density also plays an important role. Even though the density ranges over many orders of magnitude, its response to the burning rates is only linear and hence its importance is much less significant as far as elemental synthesis is concerned unless one considers a situation where low temperature and high density are prevailing. The materials are synthesized in the inner regions near the core and are brought to the surface by means of some physical mechanisms like convection or by dredge-up. Here the stars are assumed to be spherically symmetrical with no magnetic field, no rotation and no mass loss from the surface. The process of convection is the only mixing mechanism operating in the convective regions, which are always fully mixed (Salaris et al. 2002). These conditions are the canonical model of a star.

But in recent years, it has become clear that stellar evolution, particularly for more massive stars, can also be profoundly influenced by the loss of mass and angular momentum from the stellar envelope and surface (Maeder & Meynet 2008). Models of main sequence evolution in rotating massive stars show that, at the surface, the velocity approaches a critical limit. This is induced by the internal evolution of stars, which results in transport of angular momentum from the contracting, faster rotating inner convective core to the expanding, slowed down radiative envelope (Meynet et al. 2006). However beyond the critical limit, any further increase in rotation rate is not dynamically allowed, hence further contraction of the interior is then balanced by a net loss of angular momentum through induced mass loss. Here this mass loss is assumed to be isotropic. Thus synthesized mass by the star will now be delivered to the interstellar medium (ISM), and hence the ISM is pre-enriched with material that has been produced by other stars. Moreover, the materials are assumed to be released into the ISM with a very low velocity and can easily be retained in the potential well of the GC. Here we assume the density of stellar matter is constant which, in general, is not a sensitive parameter unless one goes to a high value of $\sim 10^5$ gm cc^{-1} or even higher where a pycnonuclear type of reaction has to be considered. We also assume the star to be in equilibrium, thereby making it maintain a balance between the produced energy due to thermonuclear fusion and loss of energy at the surface. Thus the temperature of the star can essentially be assumed to be a fixed quantity. Here we mainly focus on which type of star produces the material enriched in H-burning products and how. However, we neither comment on the physical factors that influence mass loss nor look for what physical mechanism is responsible for selecting only material bearing the signatures of H-processing that has been lost.

3 HYDROGEN BURNING NUCLEOSYNTHESIS

The rate of nuclear reactions is dependent on the density of the reactants, the velocity of one reactant relative

to another, and the probability of a reaction occurring. Mathematically

$$R = \frac{1}{1+\delta_{ij}} N_i N_j \langle \sigma v \rangle \,, \tag{1}$$

where i, j are two separate species and δ_{ij} is the function preventing double counting of those two species. For computational simplification, the number density N_i of any element with mass number A_i can be expressed in terms of its mass fraction X_i by $N_i = \rho X_i N_{\rm A}/A$. Here ρ is density and $N_{\rm A}$ is Avogadro's number. The thermonuclear reaction rate for a proton-capture reaction then takes the form

$$R = \frac{\rho^2 N_{\rm A}}{A_{\rm H} A_i} \Big[X_{\rm H} X_i \Big(N_{\rm A} \langle \sigma v \rangle \Big) \Big] \, {\rm cm^{-3}\, s^{-1}} \,, \tag{2}$$

where $N_{\rm A}\langle \sigma v \rangle$ is the reaction rate constant and X_i is the mass fraction of any other heavy element. From this, the lifetime against proton-capture for elements in the enhanced state is given by the following equation

$$\tau_{\rm p} = \frac{1}{\rho X_{\rm H} [N_{\rm A} \langle \sigma v \rangle]} \, {\rm s} \,. \tag{3}$$

4 CNOF CYCLE

If heavier elements are present in some stellar condition where the temperature and density are low, then the ^{12}C(p,γ)^{13}N reaction can compete with the p-p reaction and thereby can initiate the CNO burning mechanism (Clayton 1983 and references therein). ^{13}N is β unstable and decays to ^{13}C in a time scale of 862.77 s (Audi et al. 1997) since its proton capture lifetime is quite large in the considered temperature and density condition. On the other hand, ^{13}C is a stable isotope of carbon with relative abundance 1.1078 (Lodders 2003). This ^{13}C forms ^{14}N by taking a proton and then ^{14}N to ^{15}O by taking a proton again. ^{15}O then decays via a β emission to ^{15}N with an average lifetime of 176.39 s (Audi et al. 1997). Here ^{15}N branching appears. Table 1 shows the branching ratios of the cycle at various temperatures.

These branching ratios show that the (p,α) reaction wins over the (p,γ) reaction, thus confirming the cyclic behavior forming ^{12}C by most of the ^{15}N nuclei. This is CN cycling. The branching ratio will guide how much ^{15}N will go on to form ^{16}O by taking a proton. It is from this point onwards that the oxygen-fluorine reaction network starts, for which discussions are available in many places in the literature (Bethe 1997; Cameron & Kahl 2013). Here we give a brief description relevant to this work. A proton capture by ^{16}O leads to the formation of unstable ^{17}F which decays into ^{17}O. This secondary isotope of oxygen has very small relative abundance (Lodders 2003). This is probably due to the fact that ^{17}O gets destroyed via both ^{17}O (p, α)^{14}N and ^{17}O (p,γ)^{18}F; the former reaction rate is higher than the latter one at the same temperature. Thus the (p,α) reaction is also important for further evolution and starts competing with (p,γ) reactions. Inclusion of the (p,α) reaction that has also been considered here introduces another branching point in the cycle, for which the branching point ratio of (p,γ) to (p,α) has been listed in Table 1. If the cycle advances forming ^{18}F then this will be immediately followed by the ^{18}F(e^+, ν_e) ^{18}O reaction. This is because ^{18}F is unstable against β-decay, and at low density such as ρ_2 ($= \rho/10^2$ g cm^{-3}) $= 1$ and temperature $0.02 \leq T_9 < 0.1$, the p-capture lifetime of ^{18}F is very large compared to its β decay mean lifetime i.e. 9504 s (Audi et al. 1997). ^{18}O, the tertiary isotope of oxygen, has very low abundance compared to ^{16}O but greater compared to ^{17}O (Lodders 2003). From this point onwards, we adopt the reaction steps given in Hansen et al. (2004); Mountford (2013) i.e. ^{18}O (p, γ) ^{19}F. Sometimes the radiative capture on ^{18}O cannot be neglected as compared to O^{18} (p, α) ^{15}N even though the (p, α) channel is substantially stronger than (p, γ) channels. Depending upon the spin and energy of resonance, the latter can be of comparable strength (Wiescher et al. 1980). Still we have checked for possible alteration of abundances of oxygen by including a third branching point at ^{18}O. But still it does not lead us to find any significant change in the mass fraction of ^{16}O, which has been found to be consistent with the earlier report of Audouze et al. (1977) in which the author mentioned that the ^{18}O (p, γ) ^{19}F leak has little effect on CNO equilibrium abundance. For instance, the ^{16}O abundance changes by only 12% at temperatures T_9 =0.03 and 0.05 (refer to Section 4.2). Moreover, the goal of this choice is because it may improve our knowledge of lev-

Table 1 The branching ratio ($B_r = \frac{N_{\rm A}\langle \sigma v \rangle_{p,\gamma}}{N_{\rm A}\langle \sigma v \rangle_{p,\alpha}}$) at various temperatures in units of T_9. The rate constants for ^{15}N are taken from the NACRE compilation and those for ^{17}O are taken from Iliadis et al. (2010).

T_9	^{15}N(B_r)	^{17}O(B_r)
0.02	4.615×10^{-4}	1.312×10^{-1}
0.03	4.232×10^{-4}	5.601×10^{-3}
0.05	3.652×10^{-4}	4.031×10^{-3}
0.08	3.134×10^{-4}	5.745×10^{-3}
0.1	2.857×10^{-4}	7.722×10^{-3}

els in the ^{19}F nucleus that are relevant to nuclear astrophysics and hopefully for a possible fluorine production network. Recently, Buckner et al. (2012) studied the ^{18}O (p, γ) ^{19}F reaction and found that most ^{19}F levels decay by $\gamma\gamma$-cascades through the first (110 keV) excited state, and all ^{19}F levels (with known decay schemes) deexcite through the second (197 keV) excited state. It is also an interesting element in the periodic table because of the fact that though it is surrounded by some of the most abundant elements in the universe like oxygen, nitrogen and neon, it is itself very rare. Perhaps this is because it is an odd Z element with only one single stable isotope and it is very fragile with nine protons and ten neutrons (Palacois 2006). Then the finally produced ^{19}F is destroyed by a (p, α) reaction forming ^{16}O since the ^{19}F (p, α) ^{16}O (p, α) reaction rate is faster than the (p, γ) reaction which would have produced ^{20}Ne. Thus the CNOF cycle is

$$
\begin{aligned}
^{12}\mathrm{C} + p &\longrightarrow {}^{13}\mathrm{N} + \gamma \\
^{13}\mathrm{N} &\longrightarrow {}^{13}\mathrm{C} + e^{+} + \nu_e \\
^{13}\mathrm{C} + p &\longrightarrow {}^{14}\mathrm{N} + \gamma \\
^{14}\mathrm{N} + p &\longrightarrow {}^{15}\mathrm{O} + \gamma \\
^{15}\mathrm{O} &\longrightarrow {}^{15}\mathrm{N} + e^{+} + \nu_e \\
^{15}\mathrm{N} + p &\longrightarrow {}^{12}\mathrm{C} + \alpha \\
^{15}\mathrm{N} + p &\longrightarrow {}^{16}\mathrm{O} + \gamma \\
^{16}\mathrm{O} + p &\longrightarrow {}^{17}\mathrm{F} + \gamma \\
^{17}\mathrm{F} &\longrightarrow {}^{17}\mathrm{O} + e^{+} + \nu_e \\
^{17}\mathrm{O} + p &\longrightarrow {}^{14}\mathrm{N} + \alpha \\
^{17}\mathrm{O} + p &\longrightarrow {}^{18}\mathrm{F} + \gamma \\
^{18}\mathrm{F} &\longrightarrow {}^{18}\mathrm{O} + e^{+} + \nu_e \\
^{18}\mathrm{O} + p &\longrightarrow {}^{19}\mathrm{F} + \gamma \\
^{19}\mathrm{F} + p &\longrightarrow {}^{16}\mathrm{O} + \alpha
\end{aligned}
$$

To calculate the lifetimes of all the reactions at the density value, the required reaction rate constants are taken from Iliadis et al. (2010) which are the recommended medium rate constant values except for the (p, α) reactions. Reaction rate constants for the (p, α) reactions involved in this cycle have been taken from the NACRE. Estimated proton-capture lifetimes for various elements are listed in Table 2 which are relevant to our reaction cycle.

4.1 NeNa Cycle

At high temperature conditions, additional hydrogen burning cycles may come in the form of the NeNa cycle (Marion & Fowler 1957). Because of the high Coulomb barrier, they may not seem important from the perspective of energy sources. However, the enhancement of Na, which has been observationally found in many red giant and supergiant stars, demands investigation of the NeNa cycle as a possible candidate for Na enhancement. Typically this cycle starts from ^{20}Ne which captures a proton to form ^{21}Na. This unstable ^{21}Na forms ^{21}Ne via a β emission. However the reaction ^{21}Ne (α, n) ^{24}Mg can be a source of neutrons (Burbidge et al. 1957) if α particles are available but the branching ratio ($\frac{N_{\mathrm{A}}\langle\sigma v\rangle_{\alpha,n}}{N_{\mathrm{A}}\langle\sigma v\rangle_{p,\gamma}}$)$\ll 1$ guarantees the production of ^{22}Na through ^{21}Ne (p,γ) ^{22}Na which is a relatively long-lived isotope of Na with an average lifetime of 1.183×10^8 s. ^{22}Na produces ^{22}Ne via ^{22}Na (e^+, ν_e) ^{22}Ne. We have also taken into account the reaction ^{22}Na (p,γ) ^{23}Mg that may affect the energy production rate, cycle lifetime and abundance of Na. Other β-decay lifetimes cannot compete with the proton-capture lifetime so long as the value of temperature $T_9 \leq 0.05$. Production of ^{25}Mg from ^{22}Ne via (α, n) reaction is ignored as the temperature required ($T_9 = 0.3$) for this reaction to occur is beyond the temperature range we have considered. Reactions in the NeNa cycle will depend upon the competition between proton capture and β-decay lifetimes, which again in turn depend upon the density and temperature conditions. These factors are taken into account, and thus the NeNa cycle is shown below:

$$
\begin{aligned}
^{20}\mathrm{Ne} + p &\longrightarrow {}^{21}\mathrm{Na} + \gamma \\
^{21}\mathrm{Na} &\longrightarrow {}^{21}\mathrm{Ne} + e^{+} + \nu_e \\
^{21}\mathrm{Ne} + p &\longrightarrow {}^{22}\mathrm{Na} + \gamma \\
^{22}\mathrm{Na} &\longrightarrow {}^{22}\mathrm{Ne} + e^{+} + \nu_e \\
^{22}\mathrm{Ne} + p &\longrightarrow {}^{23}\mathrm{Na} + \gamma \\
^{23}\mathrm{Na} + p &\longrightarrow {}^{20}\mathrm{Ne} + \alpha
\end{aligned}
$$

Thus ^{20}Ne can be formed when ^{23}Na captures a proton as the nuclear reaction rate for ^{23}Na (p,α) ^{20}Ne is higher ($10 - 10^2$) (Iliadis et al. 2010) than the competing reaction ^{23}Na (p,γ) ^{24}Mg, which is sufficient to guarantee NeNa cycling. In Table 3 we present the proton-capture lifetimes for various elements in the considered stellar condition. The reaction rate constants are taken from Iliadis et al. (2010).

4.2 MgAl Cycle

This cycle, initiated by ^{24}Mg with a proton-capture, leads to the formation of unstable ^{25}Al. ^{24}Mg is the most abundant element of the cycle for temperature $T_9 \leq 0.05$ because of the slow reaction rate of ^{24}Mg (p,γ) ^{25}Al. ^{25}Al quickly disintegrates to ^{25}Mg in an average time scale of 10.365 s (Audi et al. 1997). ^{25}Mg through a (p, γ) reaction forms the other isotopes of Al. The first one is ^{26}Al

Table 2 Estimated proton-capture reaction lifetimes for the nuclear reactions. The rate constants $N_{\rm A}\langle\sigma v\rangle$ are in $\rm cm^3\,mol^{-1}\,s^{-1}$, T_9 is in the unit of 10^9 K and ρ_2 is in the unit of 10^2 gm cc^{-1}. The τ_β values for ^{13}N, ^{15}O, ^{17}F and ^{18}F are 862.77, 176.39, 93.059 and 9504 s respectively. τ_β and $\tau_{\rm p}$ represent the β-decay and proton-capture lifetimes respectively in second.

Reaction	T_9	$N_{\rm A}\langle\sigma v\rangle$	$\tau_{\rm p}(\rho_2=1)$
$^{12}{\rm C}(p,\gamma)^{13}{\rm N}$	0.02	3.76×10^{-14}	3.79×10^{11}
	0.03	1.74×10^{-11}	8.21×10^{8}
	0.05	1.31×10^{-8}	1.09×10^{6}
	0.08	2.28×10^{-6}	6.26×10^{3}
	0.1	2.03×10^{-5}	7.03×10^{2}
$^{13}{\rm C}(p,\gamma)^{14}{\rm N}$	0.02	1.89×10^{-13}	7.55×10^{10}
	0.03	8.77×10^{-11}	1.62×10^{8}
	0.05	6.49×10^{-8}	2.20×10^{5}
	0.08	1.10×10^{-5}	1.29×10^{3}
	0.1	9.60×10^{-5}	1.48×10^{2}
$^{13}{\rm N}(p,\gamma)^{14}{\rm O}$	0.02	4.11×10^{-16}	3.47×10^{13}
	0.03	3.85×10^{-13}	3.71×10^{10}
	0.05	6.15×10^{-9}	2.32×10^{5}
	0.08	1.93×10^{-7}	7.40×10^{4}
	0.1	2.19×10^{-5}	6.52×10^{2}
$^{14}{\rm N}(p,\gamma)^{15}{\rm O}$	0.02	1.59×10^{-16}	8.98×10^{13}
	0.03	1.45×10^{-13}	9.85×10^{10}
	0.05	2.21×10^{-10}	6.46×10^{7}
	0.08	6.50×10^{-8}	2.19×10^{5}
	0.1	7.20×10^{-7}	1.98×10^{4}
$^{15}{\rm N}(p,\gamma)^{16}{\rm O}$	0.02	3.90×10^{-15}	3.66×10^{12}
	0.03	3.70×10^{-12}	3.86×10^{9}
	0.05	5.97×10^{-9}	2.39×10^{6}
	0.08	1.89×10^{-6}	7.55×10^{3}
	0.1	2.16×10^{-5}	6.61×10^{2}
$^{15}{\rm O}(p,\gamma)^{16}{\rm F}$	0.02	5.45×10^{-47}	2.62×10^{44}
	0.03	1.25×10^{-43}	1.14×10^{41}
	0.05	6.66×10^{-37}	2.14×10^{34}
	0.08	1.34×10^{-34}	1.06×10^{32}
	0.1	4.64×10^{-33}	3.07×10^{30}
$^{16}{\rm O}(p,\gamma)^{17}{\rm F}$	0.02	3.78×10^{-18}	3.77×10^{15}
	0.03	6.59×10^{-15}	2.16×10^{12}
	0.05	1.98×10^{-11}	7.21×10^{8}
	0.08	9.71×10^{-9}	1.47×10^{6}
	0.1	1.30×10^{-7}	1.09×10^{6}
$^{17}{\rm F}(p,\gamma)^{18}{\rm Ne}$	0.02	6.12×10^{-21}	2.33×10^{18}
	0.03	2.15×10^{-17}	6.64×10^{14}
	0.05	1.36×10^{-13}	1.05×10^{11}
	0.08	1.24×10^{-10}	1.15×10^{8}
	0.1	2.17×10^{-9}	6.58×10^{6}
$^{17}{\rm O}(p,\gamma)^{18}{\rm F}$	0.02	2.08×10^{-18}	6.86×10^{15}
	0.03	9.69×10^{-15}	1.47×10^{12}
	0.05	7.62×10^{-11}	1.87×10^{8}
	0.08	1.58×10^{-8}	9.04×10^{5}
	0.1	1.39×10^{-7}	1.02×10^{5}
$^{18}{\rm F}(p,\gamma)^{19}{\rm Ne}$	0.02	5.47×10^{-17}	2.61×10^{14}
	0.03	6.84×10^{-14}	2.08×10^{11}
	0.05	2.57×10^{-11}	5.55×10^{8}
	0.08	3.88×10^{-9}	3.68×10^{6}
	0.1	3.93×10^{-8}	3.63×10^{3}
$^{18}{\rm O}(p,\gamma)^{19}{\rm F}$	0.02	1.2×10^{-17}	1.19×10^{15}
	0.03	1.79×10^{-14}	7.98×10^{11}
	0.05	1.35×10^{-10}	1.05×10^{8}
	0.08	7.11×10^{-6}	2.00×10^{3}
	0.1	3.17×10^{-4}	4.50×10^{1}
$^{19}{\rm F}(p,\alpha)^{16}{\rm O}$	0.02	3.76×10^{-17}	3.79×10^{14}
	0.03	1.33×10^{-13}	2.07×10^{9}
	0.05	8.72×10^{-10}	1.63×10^{7}
	0.08	9.71×10^{-9}	1.47×10^{6}
	0.1	1.65×10^{-5}	8.65×10^{2}

Table 3 Estimated proton-capture reaction lifetimes for the nuclear reactions. The rate constants $N_{\rm A}\langle\sigma v\rangle$ are in $\rm cm^3\ mol^{-1}\ s^{-1}$, T_9 is in the unit of 10^9 K and ρ_2 is in the unit of $10^2\ \rm gm\,cc^{-1}$. The τ_β values for ^{21}Na and ^{22}Na are 32.453 and 1.18×10^8 s respectively. $\tau_{\rm p}$ represents proton-capture lifetime as described in second.

Reaction	T_9	$N_{\rm A}\langle\sigma v\rangle$	$\tau_{\rm p}(\rho_2 = 1)$
^{20}Ne$(p,\gamma)^{21}$Na	0.02	3.07×10^{-21}	4.65×10^{20}
	0.03	1.39×10^{-19}	1.03×10^{17}
	0.05	1.15×10^{-13}	1.24×10^{11}
	0.08	1.23×10^{-10}	1.16×10^{8}
	0.1	2.29×10^{-9}	6.24×10^{6}
^{21}Na$(p,\gamma)^{22}$Mg	0.02	1.15×10^{-24}	1.24×10^{22}
	0.03	1.38×10^{-20}	1.04×10^{18}
	0.05	3.62×10^{-16}	3.95×10^{13}
	0.08	7.77×10^{-10}	1.84×10^{7}
	0.1	2.17×10^{-7}	6.58×10^{4}
^{21}Ne$(p,\gamma)^{22}$Na	0.02	5.36×10^{-22}	2.67×10^{19}
	0.03	9.42×10^{-18}	1.52×10^{15}
	0.05	3.53×10^{-10}	4.05×10^{7}
	0.08	6.45×10^{-6}	2.22×10^{3}
	0.1	1.54×10^{-4}	9.28×10^{1}
^{22}Na$(p,\gamma)^{23}$Mg	0.02	5.19×10^{-20}	2.75×10^{17}
	0.03	2.2×10^{-16}	6.49×10^{13}
	0.05	1.37×10^{-12}	1.04×10^{10}
	0.08	3.41×10^{-9}	4.19×10^{6}
	0.1	6.93×10^{-7}	2.06×10^{4}
^{22}Ne$(p,\gamma)^{23}$Na	0.02	1.96×10^{-16}	7.29×10^{13}
	0.03	1.01×10^{-13}	1.41×10^{11}
	0.05	1.15×10^{-11}	1.24×10^{9}
	0.08	3.84×10^{-10}	3.72×10^{7}
	0.1	9.18×10^{-9}	1.56×10^{6}
^{23}Na$(p,\alpha)^{20}$Ne	0.02	5.58×10^{-22}	2.56×10^{19}
	0.03	6.55×10^{-18}	2.18×10^{15}
	0.05	2.28×10^{-13}	6.27×10^{10}
	0.08	4.37×10^{-9}	3.27×10^{6}
	0.1	3.35×10^{-7}	4.26×10^{5}

which exists in two states, a ground state ^{26g}Al and an isomeric state ^{26m}Al. If temperature $T_9 \geq 1$, both ^{26g}Al ($T_\beta = 3.262 \times 10^{13}$ s; Audi et al. (1997)) and ^{26m}Al ($T_\beta = 9.155$ s; Audi et al. 1997) quickly attain equilibrium. At $T_9 \leq 0.4$ (which falls within the temperature range considered here) the equilibrium does not become established and hence both species have to be treated separately (Ward & Fowler 1980). Thus, if the temperature $T_9 < 0.03$, destruction of ^{26g}Al mainly occurs through a β-decay reaction at both density values considered here. Assuming this isotope of Al to be stable, we have considered ^{26g}Al (p, γ) ^{27}Si (e^+, ν_e) ^{27}Al in the range of temperatures. The destruction of ^{27}Al again depends upon the stellar temperature. As long as the temperature T_9 remains less than 0.08, the (p, α) reaction wins over the (p, γ) reaction (Iliadis et al. 2010) which is sufficient to confirm the cyclic nature of Mg-Al burning modes. But if T_9 goes beyond that value, there will be leakage of ^{27}Al through ^{27}Al (p, γ) ^{28}Si which is being ignored in the present case. For the MgAl cycle, the following reaction chains are being considered.

$$
\begin{aligned}
^{24}\mathrm{Mg} + p &\longrightarrow {}^{25}\mathrm{Al} + \gamma \\
^{25}\mathrm{Al} &\longrightarrow {}^{25}\mathrm{Mg} + e^+ + \nu_e \\
^{25}\mathrm{Mg} + p &\longrightarrow {}^{26g}\mathrm{Al} + \gamma \\
^{26g}\mathrm{Al} + p &\longrightarrow {}^{27}\mathrm{Si} + \gamma \\
^{27}\mathrm{Si} &\longrightarrow {}^{27}\mathrm{Al} + e^+ + \nu_e \\
^{27}\mathrm{Al} + p &\longrightarrow {}^{24}\mathrm{Mg} + \alpha
\end{aligned}
$$

The proton-capture lifetimes have been calculated for the cycle using the recommended reaction rate constants from Iliadis et al. (2010). Once again the nuclear reaction sequence in the MgAl cycle depends on the competition between proton-capture and β-decay lifetimes. Estimated proton-capture lifetimes for various elements are presented in Table 4.

4.3 Evolution of Elemental Abundances

In the reaction cycle considered, the cycle produces one α-particle along with two ν_es and two e^+s. The initial

Table 4 Estimated proton-capture reaction lifetimes for the nuclear reactions. The rate constants $N_{\rm A}\langle\sigma v\rangle$ are in $\rm cm^3\,mol^{-1}\,s^{-1}$, T_9 is in the unit of 10^9 K and ρ_2 is in the unit of 10^2 gm cc^{-1}. The τ_β values for ^{25}Al, ^{26g}Al and ^{27}Si are 10.365, 3.26×10^{13} and 6.002 s respectively. $\tau_{\rm p}$ represents the proton-capture lifetimes as described in second.

Reaction	T_9	$N_{\rm A}\langle\sigma v\rangle$	$\tau_{\rm p}(\rho_2=1)$
^{24}Mg$(p,\gamma)^{25}$Al	0.02	4.0×10^{-26}	3.57×10^{23}
	0.03	8.92×10^{-22}	1.60×10^{19}
	0.05	9.94×10^{-17}	1.44×10^{14}
	0.08	3.08×10^{-9}	4.64×10^{6}
	0.1	1.09×10^{-6}	1.31×10^{4}
^{25}Al$(p,\gamma)^{26}$Si	0.02	4.28×10^{-28}	3.34×10^{25}
	0.03	1.63×10^{-23}	8.76×10^{20}
	0.05	2.42×10^{-18}	5.90×10^{15}
	0.08	6.69×10^{-13}	2.14×10^{10}
	0.1	5.39×10^{-11}	2.65×10^{8}
^{25}Mg$(p,\gamma)^{26g}$Al	0.02	3.81×10^{-20}	3.75×10^{19}
	0.03	1.41×10^{-15}	1.01×10^{13}
	0.05	5.57×10^{-12}	2.57×10^{9}
	0.08	1.45×10^{-9}	9.85×10^{6}
	0.1	1.34×10^{-8}	1.07×10^{6}
^{26g}Al$(p,\gamma)^{27}$Si	0.02	4.78×10^{-26}	2.99×10^{23}
	0.03	1.49×10^{-19}	9.57×10^{16}
	0.05	1.25×10^{-13}	1.14×10^{11}
	0.08	7.8×10^{-10}	1.83×10^{7}
	0.1	8.17×10^{-8}	1.75×10^{5}
^{26}Mg$(p,\gamma)^{27}$Al	0.02	6.13×10^{-22}	2.33×10^{19}
	0.03	1.09×10^{-17}	1.31×10^{15}
	0.05	1.02×10^{-12}	1.40×10^{10}
	0.08	3.03×10^{-9}	4.71×10^{6}
	0.1	5.66×10^{-8}	2.52×10^{5}
^{27}Si$(p,\gamma)^{28}$P	0.02	1.78×10^{-23}	8.03×10^{20}
	0.03	6.35×10^{-20}	2.25×10^{17}
	0.05	3.26×10^{-15}	4.38×10^{12}
	0.08	7.13×10^{-11}	2.00×10^{8}
	0.1	3.82×10^{-9}	3.74×10^{6}
^{27}Al$(p,\alpha)^{24}$Mg	0.02	3.07×10^{-25}	4.65×10^{22}
	0.03	1.86×10^{-19}	7.68×10^{16}
	0.05	9.11×10^{-15}	1.57×10^{12}
	0.08	3.84×10^{-12}	3.72×10^{9}
	0.1	4.34×10^{-11}	3.29×10^{8}

nuclei act mainly as catalysts. Although there is always a consumption of hydrogen, the total mass and total number of nuclei in each cycle remain conserved. Thus the net effect for all the three cycles is

$$4^1{\rm H}\rightarrow^4{\rm He}+2e^+ +2\nu_e+\gamma,\ \frac{dN_{\rm H}}{dt}<0,\ \frac{dN_{\rm He}}{dt}>0. \quad (4)$$

The generalized differential equation that governs the evolution of any element in terms of number density via a proton-capture reaction or a β-decay, or both, at the enhanced condition is given by Clayton (1983)

$$\frac{dN_i}{dt}=-N_iN_{\rm H}\langle\sigma v\rangle_{p,i}+N_jN_{\rm H}\langle\sigma v\rangle_{H,j}\pm\lambda_kN_k, \quad (5)$$

where λ_k is the decay constant of an unstable nucleus with number density N_k. As all the three cycles involve proton-capture reactions and β-decays, the abundances will primarily depend upon the lifetime of these processes. If the β-decay lifetime τ_β for an unstable element in the cycle is shorter than the proton-capture lifetime $\tau_{\rm p}$ for the same element, then the β-decay lifetime can be bypassed and thus the element can be thought of as representing the next stable element in the cycle having the same mass number. Considering that Equation (5) for each cycle takes the form of the following differential rate equations in terms of mass fraction of any element

$$\frac{dX_i}{dt}=\left(-R_{p,i}X_iX\rho+\frac{A_i}{A_j}R_{p,j}X_jX\rho\right), \quad (6)$$

where $R_{p,i}$s are $[N_{\rm A}\langle\sigma v\rangle]$ terms for the respective proton-capture reactions. A_i and A_j stand for mass numbers of different nuclei. Equation (6) can be expressed as a function of the hydrogen mass fraction to get a series

of first order simultaneous linear differential equations for each cycle as

$$\frac{dX_i}{dX_{\rm H}} = \frac{\left(-R_{p,i}X_i + \frac{A_i}{A_j}R_{p,j}X_j\right)}{\left[-\sum_{A_i}^{A_j}\left(\frac{1}{A_i}R_{p,i}X_i\right)\right]}, \quad (7)$$

which are then solved for a suitable initial condition.

4.4 Calculation of Abundances

In the case of the CNOF cycle, the initial abundance of heavy elements has been chosen in such a manner that it does not affect the production of primary nitrogen from being the most abundant element in the CNO reaction, which actually gets hampered for metallicities higher than $Z = 0.001$. Moreover, at higher metallicities rotational mixing is not so efficient. We also do not take very or extremely low metallicities because low metallicity reveals a low content of heavy elements, thereby making the opacity lower. Hence the stars become more compact and therefore hotter, so they are going to have high luminosity. This high luminosity increases the radiation pressure and thus stellar mass loss (Meynet et al. 2009). Fast rotating massive stars, with an initial metallicity $Z = 0.0005$, with typical time averaged velocity of 500 km s^{-1} on the main sequence easily reach the critical velocity (Decressin et al. 2007b) at the beginning of their evolution and remain near the critical limit during the rest of their main sequence. As a consequence, they lose a large amount of material through a mechanical wind, which probably leads to the formation of a slow outflowing Keplerian equatorial disk. Keeping all of these factors in mind, simultaneous linear first order differential equations are solved numerically for each cycle varying the hydrogen mass fraction up to $X = 0.60$ to get the equilibrium mass fraction abundances of the stable heavy elements with the initial condition of $X = 0.70$, $Y = 0.298$, such that $X + Y + Z = 1$ where Z is the sum of the mass fraction of elements ^{12}C, ^{14}N, ^{16}O and ^{19}F distributed equally; i.e. $Z_{^{12}\rm C} = Z_{^{14}\rm N} = Z_{^{16}\rm O} = Z_{^{19}\rm F} = 0.0005$ for CNOF then $X = 0.70$, $Y = 0.2995$, $Z_{^{20}\rm Ne} = 0.0005$ for NeNa and lastly $X = 0.70$, $Y = 0.2995$, $Z_{^{24}\rm Mg} = 0.0005$ for the MgAl cycle (Meynet et al. 2008). The equilibrium abundance by mass fraction of the stable isotopes of considered elements are taken up to the first decimal place. We have also calculated the range of uncertainty in the equilibrium mass fraction abundance of ^{16}O, ^{23}Na and ^{27}Al due to uncertainty in the reaction rate constants considering both low and high rate constants for respective reactions (Iliadis et al. 2010) as well as the NACRE. These are presented in Table 5.

These abundances by mass fraction of the stable isotopes of any element (x) with respect to Fe are then calculated using the expression

$$\left[\frac{x}{\rm Fe}\right] = \left[\frac{x}{\rm H}\right] - \left[\frac{\rm Fe}{\rm H}\right]. \quad (8)$$

Here

$$\left[\frac{x}{\rm H}\right] = \log\left[\frac{N_x}{N_{\rm H}}\right]_{\rm star} - \log\left[\frac{N_x}{N_{\rm H}}\right]_{\odot},$$

and

$$\left[\frac{\rm Fe}{\rm H}\right] = \log\left[\frac{N_{\rm Fe}}{N_{\rm H}}\right]_{\rm star} - \log\left[\frac{N_{\rm Fe}}{N_{\rm H}}\right]_{\odot}.$$

The quantities $N_{x\odot}$ and $N_{\rm H\odot}$ are the solar number densities taken from Lodders (2003). For oxygen we have taken the equilibrium ^{16}O mass fraction for the abundance calculations since its relative abundance is larger compared to the other two stable isotopes of oxygen. The calculated abundances of O, Na and Al are presented in Tables 6, 7, 8 and 9, for density $\rho_2 = 1$ for the clusters M3, M4, M13 and NGC 6752 respectively. The observed abundances of a few metal poor evolved stars from Cohen & Meléndez (2005); Ivans et al. (1999); Cohen & Meléndez (2005) and Yong et al. (2005) are also presented in these tables for comparison. The calculated abundances at a particular temperature are those for which the difference between observed and calculated abundance is found to be minimum. Here most of the stars have been impacted since the influence of the wind is necessary in order to explain the GC abundance anomalies (Decressin et al. 2007b). Moreover, the second generation of stars is formed because of the ejection of material from the rapidly rotating massive stars which are mixed with primordial material left over from the star formation process (Bastian et al. 2014). A recent study conducted by Bekki (2011) has shown that in massive star clusters a second generation of stars is formed from the gaseous ejecta of AGB stars if the mass of the cluster exceeds $10^6\,M_{\odot}$. This gives the possibility for the presence of many massive stars within the same GC. A comparison between the computed and observed abundances from Cohen & Meléndez (2005); Ivans et al. (1999); Cohen & Meléndez (2005) and Yong et al. (2005) is shown in Figures 3, 4, 5 and 6 respectively. In Figure 6 the observed [O/Fe] and [Na/Fe] values have $\sigma < 0.1$ dex (Yong et al. 2005).

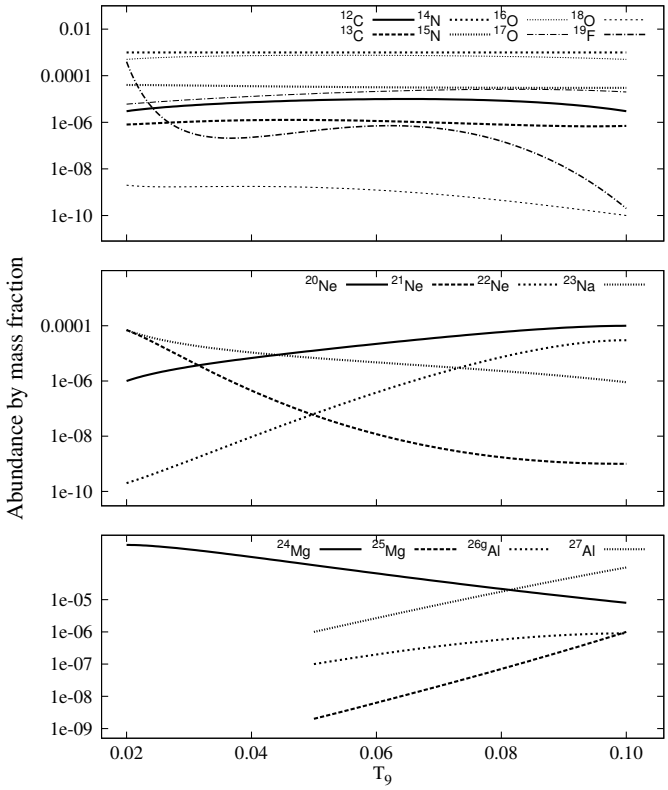

Fig. 1 Profiles of equilibrium abundances by mass fraction of stable isotopes with respect to temperature are shown for stable nuclides in the CNOF cycle (*top panel*), NeNa cycle (*middle panel*) and MgAl cycle (*bottom panel*) at density $\rho_2 = 1$ gm cc^{-1}. *Top panel*: The ^{14}N abundance is found to be highest among all cases, while the abundance of ^{16}O is higher compared to the abundances of other isotopes of oxygen, but does not show any significant variation. This is probably because these two isotopes are circulated back by ^{17}O (p, α) ^{14}N and ^{19}F (p, α) ^{16}O respectively. Middle panel: In the NeNa cycle, Na does show variation with respect to increase in temperature. This is probably directly reflected by the increase in ^{20}Ne abundance. Bottom panel: In the MgAl cycle, the elements presented here only show their effect at temperature greater than $T_9 = 0.03$ and they do show noticeable variation with respect to temperature. Abundance of ^{24}Mg decreases with respect to temperature at a steeper slope. Thus at higher temperature, more ^{25}Mg will be present which in turn will influence the production of ^{26g}Al, which also decreases slowly with the increase in temperature. These decrements result in an increase of the ^{27}Al isotope.

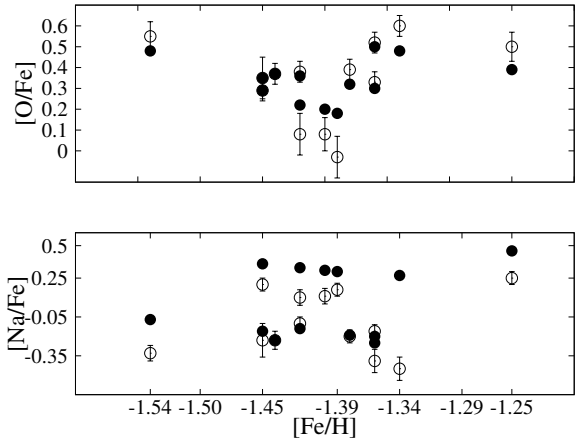

Fig. 2 A comparison between the calculated and observed abundance ratios of [O/Fe] and [Na/Fe] for GC M3. The data points are taken from Table 6. Here solid circles mean "this work" and open circles mean Yong et al. (2005).

Table 5 The estimated abundance by mass fraction of ^{16}O, ^{23}Na and ^{27}Al due to uncertainty in the reaction rate constants with low, medium (recommended) and high reaction rate constant.

T_9	^{16}O			^{23}Na			^{27}Al		
	Low	Medium	High	Low	Medium	High	Low	Medium	High
0.02	5×10^{-4}	5×10^{-4}	5×10^{-4}	6×10^{-5}	7×10^{-5}	1×10^{-4}	****	*****	*****
0.03	6×10^{-4}	8×10^{-4}	6×10^{-4}	1×10^{-5}	1×10^{-5}	5×10^{-6}	****	*****	*****
0.05	7×10^{-4}	8×10^{-4}	8×10^{-4}	1×10^{-5}	6×10^{-6}	6×10^{-6}	3×10^{-6}	1×10^{-6}	8×10^{-7}
0.08	7×10^{-4}	8×10^{-4}	8×10^{-4}	3×10^{-6}	3×10^{-6}	4×10^{-6}	2×10^{-5}	2×10^{-5}	2×10^{-5}
0.10	8×10^{-4}	5×10^{-4}	8×10^{-4}	1×10^{-6}	9×10^{-7}	1×10^{-6}	4×10^{-5}	1×10^{-5}	2×10^{-5}

Table 6 The Estimated Abundance Ratios of [O/Fe] and [Na/Fe] for GC M3

Star	$\left[\frac{\rm Fe}{\rm H}\right]^a$	$\left[\frac{\rm O}{\rm Fe}\right]^a$	$\left[\frac{\rm Na}{\rm Fe}\right]^a$	$\left[\frac{\rm O}{\rm Fe}\right]^b$	$\left[\frac{\rm Na}{\rm Fe}\right]^b$
VZ1397	-1.36	$0.52\pm0.05^*$	-0.16 ± 0.05	$+0.50$	-0.20
II-46	-1.44	$0.37\pm0.05^*$	-0.23 ± 0.07	$+0.37$	-0.23
VZ1000	-1.42	0.08 ± 0.10	$+0.10\pm0.06$	$+0.22$	$+0.33$
III-28	-1.54	0.55 ± 0.07	-0.33 ± 0.06	$+0.48$	-0.07
IV-25	-1.42	$0.38\pm0.05^*$	-0.10 ± 0.05	$+0.36$	-0.14
C41303-2217	-1.36	$0.33\pm0.05^*$	-0.39 ± 0.09	$+0.30$	-0.25
IV-27	-1.40	0.08 ± 0.08	$+0.11\pm0.06$	$+0.20$	$+0.31$
III-61	-1.34	0.60 ± 0.05	-0.45 ± 0.09	$+0.48$	$+0.27$
III-60	-1.45	$0.29\pm0.05^*$	-0.23 ± 0.13	$+0.29$	-0.16
C41544-2336	-1.38	$0.39\pm0.05^*$	$-0.20\pm0.05^*$	$+0.32$	-0.19
V-30	-1.39	$<-0.03\pm0.10$	$+0.16\pm0.05^*$	$+0.18$	$+0.30$
V-31	-1.45	0.35 ± 0.10	$+0.20\pm0.05^*$	$+0.35$	$+0.36$
C41543-2334	-1.25	0.50 ± 0.07	$+0.25\pm0.05^*$	$+0.39$	$+0.46$

Notes: ^{a} Cohen & Meléndez (2005); ^{b} this work.

Table 7 The Estimated Abundance Ratios of [O/Fe], [Na/Fe] and [Al/Fe] for GC M4

Star	$\left[\frac{\rm Fe}{\rm H}\right]^a$	$\left[\frac{\rm O}{\rm Fe}\right]^a$	$\left[\frac{\rm Na}{\rm Fe}\right]^a$	$\left[\frac{\rm Al}{\rm Fe}\right]^a$	$\left[\frac{\rm O}{\rm Fe}\right]^b$	$\left[\frac{\rm Na}{\rm Fe}\right]^b$	$\left[\frac{\rm Al}{\rm Fe}\right]^b$
L4611	-1.16	$+0.06\pm0.03$	$+0.33\pm0.05$	$+0.60\pm0.03$	$+0.05$	$+0.37$	$+0.66$
L4613	-1.17	$+0.05\pm0.03$	$+0.26\pm0.05$	$+0.63\pm0.03$	$+0.06$	$+0.38$	$+0.67$
L1514	-1.16	$+0.41\pm0.03$	$+0.01\pm0.05$	$+0.44\pm0.03$	$+0.40$	$+0.07$	$+0.66$
L1411	-1.20	$+0.20\pm0.03$	$+0.43\pm0.05$	$+0.79\pm0.03$	$+0.19$	$+0.42$	$+0.75$
L3209	-1.20	$+0.27\pm0.03$	$+0.23\pm0.05$	$+0.71\pm0.03$	$+0.23$	$+0.16$	$+0.71$
L2307	-1.19	$+0.17\pm0.03$	$+0.39\pm0.05$	$+0.73\pm0.03$	$+0.17$	$+0.40$	$+0.73$
L2406	-1.19	$+0.19\pm0.03$	$+0.31\pm0.05$	$+0.55\pm0.03$	$+0.17$	$+0.40$	$+0.69$
L4511	-1.18	$+0.23\pm0.03$	$+0.44\pm0.05$	$+0.83\pm0.03$	$+0.21$	$+0.44$	$+0.73$
L1501	-1.20	$+0.10\pm0.03$	$+0.42\pm0.05$	$+0.81\pm0.03$	$+0.09$	$+0.42$	$+0.75$
L3413	-1.17	$+0.40\pm0.03$	-0.04 ± 0.05	$+0.61\pm0.03$	$+0.41$	$+0.08$	$+0.67$
L2617	-1.17	$+0.01\pm0.03$	$+0.50\pm0.05$	$+0.84\pm0.03$	$+0.03$	$+0.43$	$+0.72$
L3624	-1.16	$+0.29\pm0.03$	$+0.10\pm0.05$	$+0.69\pm0.03$	$+0.32$	$+0.10$	$+0.68$
L3612	-1.19	$+0.10\pm0.03$	$+0.47\pm0.05$	$+0.77\pm0.03$	$+0.08$	$+0.45$	$+0.74$
L2206	-1.18	$+0.31\pm0.03$	$+0.25\pm0.05$	$+0.69\pm0.03$	$+0.34$	$+0.39$	$+0.69$
L2208	-1.17	$+0.36\pm0.03$	$+0.55\pm0.05$	$+0.90\pm0.03$	$+0.37$	$+0.60$	$+0.97$
L2519	-1.16	$+0.37\pm0.03$	-0.19 ± 0.05	$+0.50\pm0.03$	$+0.36$	$+0.07$	$+0.66$
L4201	-1.18	$+0.41\pm0.03$	$+0.31\pm0.05$	$+0.55\pm0.03$	$+0.42$	$+0.39$	$+0.68$
L4633	-1.19	$+0.33\pm0.03$	-0.03 ± 0.05	$+0.59\pm0.03$	$+0.35$	$+0.10$	$+0.69$
L1408	-1.20	$+0.24\pm0.03$	$+0.18\pm0.05$	$+0.47\pm0.03$	$+0.23$	$+0.16$	$+0.70$
L4414	-1.15	$+0.16\pm0.03$	$+0.21\pm0.05$	$+0.70\pm0.03$	$+0.14$	$+0.36$	$+0.70$
L1701	-1.20	$+0.49\pm0.03$	-0.02 ± 0.05	$+0.62\pm0.03$	$+0.44$	$+0.11$	$+0.70$
L3207	-1.17	$+0.45\pm0.03$	-0.23 ± 0.05	$+0.37\pm0.03$	$+0.41$	-0.39	$+0.67$
L3215	-1.20	$+0.27\pm0.03$	-0.03 ± 0.05	$+0.47\pm0.03$	$+0.23$	$+0.11$	$+0.70$
L4302	-1.19	$+0.20\pm0.03$	$+0.31\pm0.05$	$+0.48\pm0.03$	$+0.17$	$+0.40$	$+0.69$

Notes: ^{a} Ivans et al. (1999); ^{b} this work.

Table 8 The Estimated Abundance Ratios of [O/Fe], [Na/Fe] and [Al/Fe] for GC M13

Star	$\left[\frac{\mathrm{Fe}}{\mathrm{H}}\right]^a$	$\left[\frac{\mathrm{O}}{\mathrm{Fe}}\right]^a$	$\left[\frac{\mathrm{Na}}{\mathrm{Fe}}\right]^a$	$\left[\frac{\mathrm{Al}}{\mathrm{Fe}}\right]^a$	$\left[\frac{\mathrm{O}}{\mathrm{Fe}}\right]^b$	$\left[\frac{\mathrm{Na}}{\mathrm{Fe}}\right]^b$	$\left[\frac{\mathrm{Al}}{\mathrm{Fe}}\right]^b$
II-67	-1.30	-1.14 ± 0.10	0.32 ± 0.05	0.64 ± 0.10	$+0.10$	$+0.26$	$+0.80$
IV-25	-1.41	$-0.33 \pm 0.05^*$	0.41 ± 0.09	0.85 ± 0.10	$+0.21$	$+0.37$	$+0.91$
II-76	-1.53	$0.55 \pm 0.05^*$	-0.32 ± 0.05	≤ 0.59	$+0.63$	-0.08	-0.22
III-18	-1.45	0.55 ± 0.10	0.36 ± 0.06	0.74 ± 0.10	$+0.55$	$+0.36$	$+0.95$
K-188	-1.45	0.33 ± 0.07	$-0.08 \pm 0.05^*$	≤ 0.57	$+0.35$	-0.11	-0.30
III-7	-1.53	0.46 ± 0.08	$0.10 \pm 0.05^*$	≤ 0.70	$+0.46$	-0.03	-0.22
I-18	-1.47	0.17 ± 0.10	$0.32 \pm 0.05^*$	≤ 0.76	$+0.27$	$+0.38$	$+0.97$
I-49	-1.49	$0.58 \pm 0.05^*$	$0.00 \pm 0.05^*$	≤ 0.67	$+0.59$	-0.07	$+0.99$
J37	-1.48	0.15 ± 0.10	0.37 ± 0.06	≤ 0.97	$+0.28$	$+0.39$	$+0.98$
C41196-2632	-1.48	-0.01 ± 0.10	$0.17 \pm 0.05^*$	...	$+0.28$	$+0.39$	...
II-4	-1.55	0.26 ± 0.10	$0.28 \pm 0.05^*$	...	$+0.35$	$+0.46$	...
IV-29	-1.49	0.52 ± 0.10	$-0.33 \pm 0.05^*$	...	$+0.59$	-0.07	...
J45	-1.47	0.16 ± 0.10	$0.18 \pm 0.05^*$	...	$+0.27$	$+0.38$	...
I-5	-1.55	...	$0.49 \pm 0.05^*$	...	...	$+0.49$	...
C41155-3103	-1.50	-0.06 ± 0.10	$0.35 \pm 0.05^*$	...	$+0.30$	$+0.41$	...
C41148-3103	-1.51	$0.55 \pm 0.05^*$	$-0.09 \pm 0.05^*$	...	$+0.61$	-0.09	...
C41134-3056	-1.40	$0.24 \pm 0.05^*$	$-0.02 \pm 0.07^*$	...	$+0.24$	-0.16	...
C40559-2839	-1.55	0.37 ± 0.06	0.15 ± 0.08	...	$+0.36$	-0.01	...
C41101-3050	-1.44	0.37 ± 0.10	$0.18 \pm 0.05^*$	...	$+0.37$	$+0.35$	...
C41099-3046	-1.36	$0.19 \pm 0.05^*$	$0.04 \pm 0.05^*$	...	$+0.49$	$+0.27$	...
C41135-3053	-1.47	$0.35 \pm 0.05^*$	$-0.05 \pm 0.05^*$	...	$+0.37$	-0.09	...
C41133-2750	-1.53	$0.26 \pm 0.05^*$	-0.04 ± 0.10	...	$+0.33$	-0.03	...
C40535-2819	-1.55	0.38 ± 0.07	0.05 ± 0.06	...	$+0.38$	-0.01	...
C40539-2813	-1.61	0.25 ± 0.07	$0.31 \pm 0.05^*$	...	$+0.41$	$+0.52$	...
C41135-2753	-1.72	0.14 ± 0.13	0.30 ± 0.10	...	$+0.62$	$+0.16$	...

Notes: ^{a} Cohen & Meléndez (2005), ^{b} this work.

5 DISCUSSION AND CONCLUDING REMARKS

Synthesis due to the proton-capture reaction has been investigated using updated reaction rates (Iliadis et al. 2010) for nuclear reaction cycles CNOF, NeNa and MgAl under conditions of high temperature and low density.

The first consequence we observe is the production of an important amount of primary ^{14}N. Our calculation yields the highest production of this element with mass fraction 0.001 (Fig. 1) which is the same order of magnitude as a stellar model with mass 60 $M_\odot$, $Z = 5 \times 10^{-4}$ and initial rotational velocity 800 km s^{-1} (Decressin et al. 2007b).

Abundance ratios, i.e., [O/Fe], [Na/Fe] and [Al/Fe], are also calculated and compared with their counterparts observed in a sample of metal poor stars in GCs M3, M4, M13 and NGC 6752 (Figs. 2, 3, 4 and 5 respectively). This comparison demonstrates the extent to which these nuclear reaction cycles can explain the observed abundances of O, Na and Al. These ratios show similar trends for stars of all the four GCs considered here. We find that within the temperature and density conditions considered, there is a small range of temperature values at which the computed [O/Fe], [Na/Fe] and [Al/Fe] ratios agree well with the observed ratios in a sample of stars of GCs M3, M4, M13 and NGC 6752.

GC stars are known to show Na-O anti-correlation. This anti-correlation is a common feature for GCs in the range of metallicity ($-2.5 \leq [\mathrm{Fe/H}] \leq -1$). To examine this effect, we have plotted the computed [Na/Fe] vs. [O/Fe] and compared with observations (Fig. 6). The computed abundance ratios are found to follow similar trends for all the GCs. We have also produced the Na-O anti-correlation range $-0.80 \leq [\mathrm{Na/O}] \leq 0.40$ collectively for all the four clusters, which is well within the comparable range observed of $-0.62 \leq [\mathrm{Na/O}] \leq 1$ (Decressin et al. 2007a). Probably a more accurate result can be obtained if one considers the ^{23}Na $(p,\alpha)^{20}$Ne reaction rate lowered by a factor of 2 for non-solar-scaled metallicity (Ventura & D'Antona 2006). Moreover, recently Buckner et al. (2012) reported an updated set of ^{18}O $(p,\gamma)^{19}$F reaction rate constants which may again give even more fine tuned results.

We have also found that the ^{24}Mg mass fraction abundance is in the same order of magnitude as the values reported in table 3 of Decressin et al. (2007b) which falls well within the considered temperature range.

Here also we did not find any anti-correlation between Mg and Al, which is similar to the kind of result

Table 9 The Estimated Abundance Ratios of [O/Fe], [Na/Fe] and [Al/Fe] for NGC 6752

Star	$\left[\frac{\mathrm{Fe}}{\mathrm{H}}\right]^a$	$\left[\frac{\mathrm{O}}{\mathrm{Fe}}\right]^a$	$\left[\frac{\mathrm{Na}}{\mathrm{Fe}}\right]^a$	$\left[\frac{\mathrm{Al}}{\mathrm{Fe}}\right]^a$	$\left[\frac{\mathrm{O}}{\mathrm{Fe}}\right]^b$	$\left[\frac{\mathrm{Na}}{\mathrm{Fe}}\right]^b$	$\left[\frac{\mathrm{Al}}{\mathrm{Fe}}\right]^b$
NGC 6752-mg0	−1.62	0.71	0.67	1.08	0.72	0.58	1.12
NGC 6752-mg1	−1.60	0.46	0.38	0.82	0.51	0.73	1.10
NGC 6752-mg2	−1.59	0.55	0.19	0.77	0.54	0.03	1.09
NGC 6752-mg3	−1.60	0.47	0.22	0.77	0.46	0.07	1.10
NGC 6752-mg4	−1.60	0.38	0.29	0.90	0.40	0.51	1.10
NGC 6752-mg5	−1.59	0.42	0.32	0.74	0.42	0.03	1.09
NGC 6752-mg6	−1.59	0.60	0.13	0.57	0.54	0.03	1.09
NGC 6752-mg8	−1.68	0.40	0.34	0.74	0.48	0.12	1.18
NGC 6752-mg9	−1.63	0.47	0.28	0.77	0.47	0.76	1.13
NGC 6752-mg10	−1.63	0.44	0.28	0.78	0.44	0.07	1.13
NGC 6752-mg12	−1.62	0.66	−0.09	0.09	0.72	0.53	−0.13
NGC 6752-mg15	−1.60	0.40	0.31	0.72	0.40	0.51	1.10
NGC 6752-mg18	−1.60	0.46	0.19	0.59	0.46	0.04	1.10
NGC 6752-mg21	−1.60	0.01	0.57	1.18	0.40	0.56	1.15
NGC 6752-mg22	−1.61	0.19	0.63	0.99	0.41	0.57	1.11
NGC 6752-mg24	−1.63	0.65	−0.09	0.12	0.58	0.02	−0.12
NGC 6752-mg25	−1.60	0.59	0.14	0.51	0.55	0.04	−0.15
NGC 6752-0	−1.62	−0.15	0.55	1.33	0.42	0.54	1.42
NGC 6752-1	−1.58	0.57	0.08	0.32	0.53	0.02	−0.17
NGC 6752-2	−1.59	−0.09	0.60	1.18	0.39	0.55	1.14
NGC 6752-3	−1.64	0.70	−0.04	0.22	0.74	0.03	−0.11
NGC 6752-4	−1.61	−0.04	0.61	1.20	0.41	0.57	1.16
NGC 6752-6	−1.61	0.09	0.54	0.96	0.41	0.53	1.11
NGC 6752-7	−1.84	0.90	0.02	0.19	0.94	0.23	0.09
NGC 6752-8	−1.62	0.66	−0.01	0.48	0.72	0.01	1.12
NGC 6752-9	−1.63	0.65	−0.02	0.13	0.41	0.02	−0.12
NGC 6752-10	−1.60	−0.02	0.65	1.06	0.40	0.56	1.10
NGC 6752-11	−1.64	0.37	0.35	0.90	0.44	0.55	1.14
NGC 6752-12	−1.62	0.29	0.27	0.41	0.42	0.06	−0.13
NGC 6752-15	−1.61	0.65	−0.10	0.58	0.56	0.00	1.11
NGC 6752-16	−1.60	0.09	0.36	0.83	0.40	0.51	1.10
NGC 6752-19	−1.61	0.29	0.22	0.59	0.41	0.05	1.11
NGC 6752-20	−1.59	0.08	0.67	1.15	0.39	0.55	1.14
NGC 6752-21	−1.61	0.49	0.29	0.63	0.47	0.05	1.11
NGC 6752-23	−1.62	0.11	0.59	1.25	0.42	0.58	1.17
NGC 6752-24	−1.65	0.56	0.01	0.36	0.56	0.04	−0.10
NGC 6752-29	−1.64	0.51	−0.07	0.35	0.50	0.03	−0.11
NGC 6752-30	−1.62	0.61	0.15	0.56	0.57	0.06	1.12

Notes: ^{a} Yong et al. (2005); ^{b} this work.

obtained in Decressin et al. (2007b). However we did not investigate the reason for such an observation. Decressin et al. (2007b) reported that the ^{24}Mg $(p,\gamma)^{25}$Al reaction rate increment could possibly lead to such an observation.

We also observe that the ^{16}O mass fraction estimated in our calculation has the same order of magnitude as that of the mean mass fraction in winds reported in table 5 of Decressin et al. (2007b) at the end of the central H burning. We also find that the ^{23}Na has the same order of magnitude (Table 5), when compared with table 5 of Decressin et al. (2007b), but these orders are closer to the mass fraction obtained if one uses the high reaction rate constants in the reaction networks. As far as ^{27}Al is concerned, we find that at temperatures greater than $T_9 = 0.05$ our estimated orders are almost 10 times greater than those estimated by Decressin et al. (2007b).

The major uncertainties present are the poorly known influence of molecular weight gradients on the shear instabilities and our ignorance of the effect of magnetic fields in the stellar interior on the transport of chemical and angular momentum, which are still being considered as prime candidates for affecting the abundance pattern. A star rotating axially, at low metallicity, triggers many instabilities in its stellar interior. These instabilities participate in the transport of chemical species and of angular momentum. Among these instabilities, shear mixing and horizontal turbulence are important agents

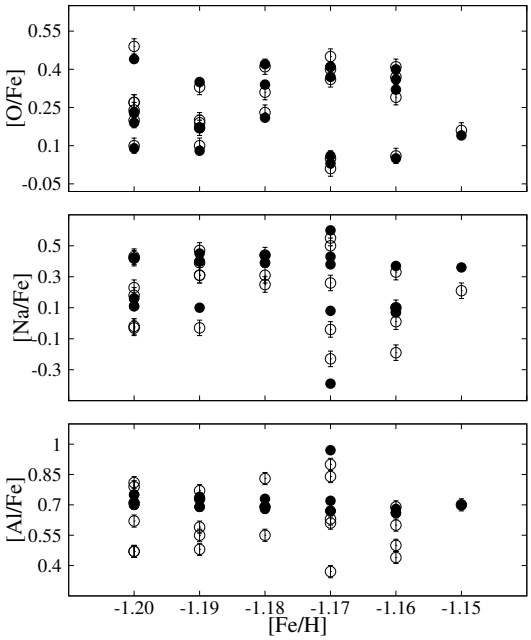

Fig. 3 A comparison between the calculated and observed abundance ratios of [O/Fe], [Na/Fe] and [Al/Fe] for GC M4. The data points are taken from Table 7. Here solid circles mean "this work" and open circles mean Ivans et al. (1999).

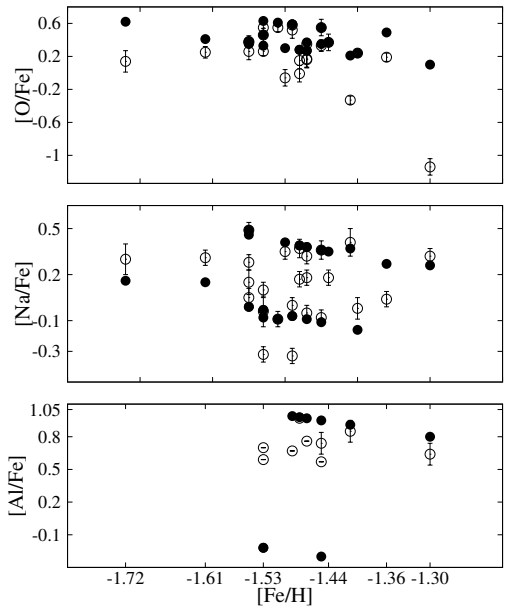

Fig. 4 A comparison between the calculated and observed abundance ratios of [O/Fe], [Na/Fe] and [Al/Fe] for GC M13. The data points are taken from Table 8. Here solid circles mean "this work" and open circles mean Cohen & Meléndez (2005).

for effective transport of chemical elements and angular momentum since in a low metallicity star rotational mixing plays a dominant role (Meynet 2008). Moreover we have considered the cyclic behavior of reaction networks, i.e., the evolution of elements is confined. However, there may also be some leakage of ^{19}F going to ^{20}Ne via a proton-capture, ^{23}Na (p,γ) ^{24}Mg (Cavallo et al. 1998) and finally ^{27}Al takes a proton resulting in the formation of ^{28}Si. This will definitely alter the abundance profile of the considered elements. The possibilities of other internal pollution mechanisms (D'Orazi et al. 2013) within the cluster are also likely to affect the abundance pattern. Theoretical uncertainties are also likely to remain, especially in the calculation of reaction rates (Iliadis et al. 2010), and the choice of the initial condition. Also, the mass loss in rotating stars is thus an asymmetric phe-

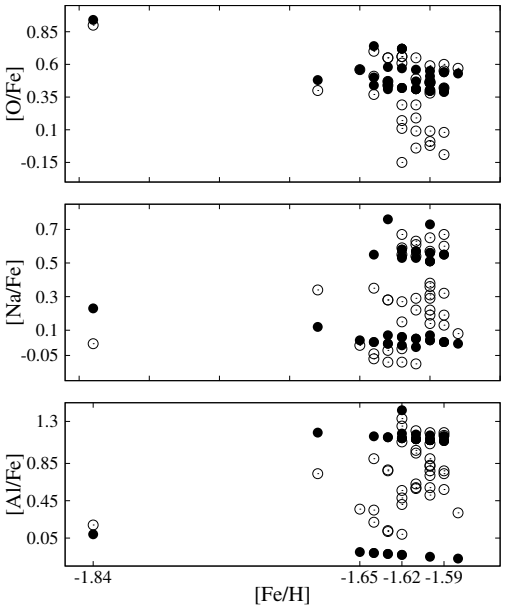

Fig. 5 A comparison between the calculated and observed abundance ratios of [O/Fe], [Na/Fe] and [Al/Fe] for NGC 6752. The data points are taken from Table 9. Here solid circles mean "this work" and open circles mean Yong et al. (2005).

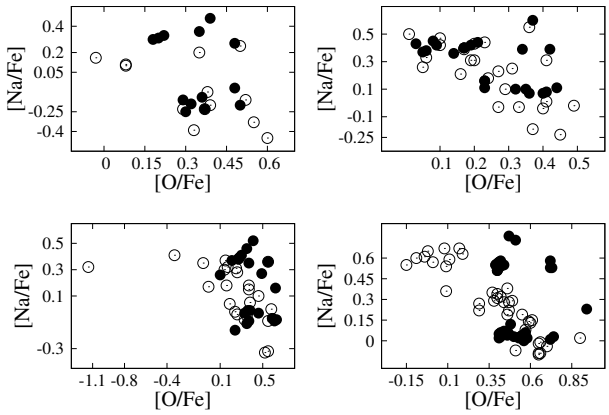

Fig. 6 Observed Na-O relation. Computed ratios in the [Na/Fe] vs. [O/Fe] plot are compared with their counterparts observed in the evolved stars of all four GCs: M3 (*top left*), M4 (*top right*), M13 (*bottom left*) and NGC 6752 (*bottom right*). We observe signs of anticorrelation between Na and O for M3, M4, M13 and NGC 6752. Here solid circles correspond to the data points of "this work" and open circles are for Cohen & Meléndez (2005) (*top left*), Ivans et al. (1999) (*top right*), Cohen & Meléndez (2005) (*bottom left*) and Yong et al. (2005) (*bottom right*).

nomenon. Very hot stars have dominant polar ejection whereas stars with temperature $< 24\,000\,\mathrm{K}$ eject most of their material through equatorial ejection, forming a disk which removes a lot of mass from the star as compared to polar ejection, even though mass loss does not play a dominant role in low metallicity stars (Meynet 2008). Nevertheless, the elements that are formed following proton-capture synthesis may have been brought to the surface which carry angular momentum with them and which is why the stars get their rotational motion. Once the rotational speed reaches a critical value, the stars start to lose their mass in the form of these synthesized materials into outer space, thus enriching the space by these materials from which the second generation stars are formed. Thus, the computed abundances of elements in the present set of initial conditions do not deviate much from the observed values of [O/Fe], [Na/Fe] and [Al/Fe] ratios. These results support the possibility that these nuclear cycles occur in such kind of a stellar situation at high temperature and low density conditions, and thus also supporting the *primordial scenario*.

Acknowledgements The author wishes to thank Prof. M.P. Bora and Dr. Bhim Prasad Sharma for their help while completing the manuscript.

References

Arnould, M., Goriely, S., & Jorissen, A. 1999, A&A, 347, 572

Audi, G., Bersillon, O., Blachot, J., & Wapstra, A. 1997, Nuclear Physics A, 624, 1

Audouze, J., Lequeux, J., Rocca-Volmerange, B., & Vigroux, L. 1977, in Astrophysics and Space Science Library, 67, CNO Isotopes in Astrophysics, ed. J. Audouze, 155

Bastian, N., Hollyhead, K., & Cabrera-Ziri, I. 2014, MNRAS, 445, 378

Bekki, K. 2011, MNRAS, 412, 2241

Bethe, H. A. 1997, Selected Works of Hans a Bethe (with Commentary) (World Scientific Publishing Co)

Buckner, M. Q., Iliadis, C., Cesaratto, J. M., et al. 2012, Phys. Rev. C, 86, 065804

Burbidge, E. M., Burbidge, G. R., Fowler, W. A., & Hoyle, F. 1957, Reviews of Modern Physics, 29, 547

Cameron, A. G. W., & Kahl, D. M. 2013, Stellar Evolution, Nuclear Astrophysics, and Nucleogenesis, ed. Kahl, D. M., with a new Introduction by Jose, J. (2nd eds., Dover Publication Inc. Mineola, NewYork)

Carretta, E., Bragaglia, A., Gratton, R. G., et al. 2009, A&A, 505, 117

Cavallo, R. M., Sweigart, A. V., & Bell, R. A. 1998, ApJ, 492, 575

Clayton, D. D. 1983, Principles of Stellar Evolution and Nucleosynthesis (Chicago: University of Chicago Press)

Cohen, J. G., & Meléndez, J. 2005, AJ, 129, 303

Cordero, M. J., Pilachowski, C. A., Johnson, C. I., & Vesperini, E. 2015, ApJ, 800, 3

D'Antona, F., & Ventura, P. 2007, MNRAS, 379, 1431

de Mink, S. E., Pols, O. R., Langer, N., & Izzard, R. G. 2009, A&A, 507, L1

Decressin, T., Charbonnel, C., & Meynet, G. 2007a, A&A, 475, 859

Decressin, T., Meynet, G., Charbonnel, C., Prantzos, N., & Ekström, S. 2007b, A&A, 464, 1029

Decressin, T., Baumgardt, H., Charbonnel, C., & Kroupa, P. 2010, A&A, 516, A73

Denissenkov, P. A., & Herwig, F. 2003, ApJ, 590, L99

D'Ercole, A., Vesperini, E., D'Antona, F., McMillan, S. L. W., & Recchi, S. 2008, MNRAS, 391, 825

Dixon, R. I., & Longmore, A. J. 1993, MNRAS, 265, 395

D'Orazi, V., Lucatello, S., Lugaro, M., et al. 2013, ApJ, 763, 22

Drake, J. J., Smith, V. V., & Suntzeff, N. B. 1992, ApJ, 395, L95

Drake, J. J., Smith, V. V., & Suntzeff, N. B. 1994, ApJ, 430, 610

Gratton, R., Sneden, C., & Carretta, E. 2004, ARA&A, 42, 385

Hansen, C. J., Kawaler, S. D., & Trimble, V. 2004, Stellar Interiors : Physical Principles, Structure, and Evolution (New York: Springer-Verlag)

Iliadis, C., Longland, R., Champagne, A. E., Coc, A., & Fitzgerald, R. 2010, Nuclear Physics A, 841, 31

Ivans, I. I., Sneden, C., Kraft, R. P., et al. 1999, AJ, 118, 1273

José, J., Coc, A., & Hernanz, M. 1999, ApJ, 520, 347

Kraft, R. P., Sneden, C., Smith, G. H., et al. 1997, AJ, 113, 279

Liu, T., & Janes, K. A. 1990, ApJ, 360, 561

Lodders, K. 2003, ApJ, 591, 1220

Maeder, A., & Meynet, G. 2008, in Revista Mexicana de Astronomia y Astrofisica Conference Series, 33, 38

Marino, A. F., Villanova, S., Piotto, G., et al. 2008, A&A, 490, 625

Marion, J. B., & Fowler, W. A. 1957, ApJ, 125, 221

Martell, S. L., Smolinski, J. P., Beers, T. C., & Grebel, E. K. 2011, A&A, 534, A136

Meynet, G., Ekström, S., & Maeder, A. 2006, A&A, 447, 623

Meynet, G. 2008, in EAS Publications Series, 32, EAS Publications Series, ed. C. Charbonnel & J.-P. Zahn, 187

Meynet, G., Decressin, T., & Charbonnel, C. 2008, Mem. Soc. Astron. Italiana, 79, 584

Meynet, G., Ekström, S., Georgy, C., Chiappini, C., & Maeder, A. 2009, in Reviews in Modern Astronomy, 21, Reviews in Modern Astronomy, ed. S. Röser, 97

Mountford, D. J. 2013, Investigations of Nuclear Reactions Relevant to Stellar γ-ray Emission, PhD Thesis, The University of Edinburgh

Palacois, A. 2006, in Stars and Nuclei: A Tribute to Manuel Forestini, 19, EAS Publications Series, ed. T. Montmerle & C. Kahane, 67

Roederer, I. U., Mateo, M., Bailey, J. I., et al. 2016, MNRAS, 455, 2417

Salaris, M., Cassisi, S., & Weiss, A. 2002, PASP, 114, 375

Sana, H., de Koter, A., de Mink, S. E., et al. 2013, A&A, 550, A107

Smolinski, J. P., Martell, S. L., Beers, T. C., & Lee, Y. S. 2011, AJ, 142, 126

Spite, M., Spite, F., Gallagher, A. J., et al. 2016, A&A, 594, A79

Vanbeveren, D., Mennekens, N., & De Greve, J. P. 2012, A&A, 543, A4

Ventura, P., & D'Antona, F. 2006, A&A, 457, 995

Ventura, P., Di Criscienzo, M., Carini, R., & D'Antona, F. 2013, MNRAS, 431, 3642

Villanova, S., Monaco, L., Moni Bidin, C., & Assmann, P. 2016, MNRAS, 460, 2351

Ward, R. A., & Fowler, W. A. 1980, ApJ, 238, 266

Wiescher, M., Becker, H. W., Görres, J., et al. 1980, Nuclear Physics A, 349, 165

Yong, D., Grundahl, F., Nissen, P. E., Jensen, H. R., & Lambert, D. L. 2005, A&A, 438, 875